



Article

CFD Study of Dual Fuel Combustion in a Research Diesel Engine Fueled by Hydrogen

Maria Cristina Cameretti ¹, Roberta De Robbio ^{1,*} , Ezio Mancaruso ²  and Marco Palomba ¹

¹ Department of Industrial Engineering, University of Naples Federico II, Via Claudio 21, 80125 Naples, Italy; mc.cameretti@unina.it (M.C.C.); marco.palomba3@studenti.unina.it (M.P.)

² STEMS—CNR, Viale G. Marconi 4, 80125 Naples, Italy; ezio.mancaruso@stems.cnr.it

* Correspondence: roberta.derobbio@unina.it

Abstract: Superior fuel economy, higher torque and durability have led to the diesel engine being widely used in a variety of fields of application, such as road transport, agricultural vehicles, earth moving machines and marine propulsion, as well as fixed installations for electrical power generation. However, diesel engines are plagued by high emissions of nitrogen oxides (NO_x), particulate matter (PM) and carbon dioxide when conventional fuel is used. One possible solution is to use low-carbon gaseous fuel alongside diesel fuel by operating in a dual-fuel (DF) configuration, as this system provides a low implementation cost alternative for the improvement of combustion efficiency in the conventional diesel engine. An initial step in this direction involved the replacement of diesel fuel with natural gas. However, the consequent high levels of unburned hydrocarbons produced due to non-optimized engines led to a shift to carbon-free fuels, such as hydrogen. Hydrogen can be injected into the intake manifold, where it premixes with air, then the addition of a small amount of diesel fuel, auto-igniting easily, provides multiple ignition sources for the gas. To evaluate the efficiency and pollutant emissions in dual-fuel diesel-hydrogen combustion, a numerical CFD analysis was conducted and validated with the aid of experimental measurements on a research engine acquired at the test bench. The process of ignition of diesel fuel and flame propagation through a premixed air-hydrogen charge was represented the Autoignition-Induced Flame Propagation model included ANSYS-Forte software. Because of the inefficient operating conditions associated with the combustion, the methodology was significantly improved by evaluating the laminar flame speed as a function of pressure, temperature and equivalence ratio using Chemkin-Pro software. A numerical comparison was carried out among full hydrogen, full methane and different hydrogen-methane mixtures with the same energy input in each case. The use of full hydrogen was characterized by enhanced combustion, higher thermal efficiency and lower carbon emissions. However, the higher temperatures that occurred for hydrogen combustion led to higher NO_x emissions.

Keywords: diesel engine; dual fuel; hydrogen; combustion modeling; CFD



Citation: Cameretti, M.C.; De Robbio, R.; Mancaruso, E.; Palomba, M. CFD Study of Dual Fuel Combustion in a Research Diesel Engine Fueled by Hydrogen. *Energies* **2022**, *15*, 5521. <https://doi.org/10.3390/en15155521>

Academic Editor: Constantine D. Rakopoulos

Received: 8 July 2022

Accepted: 25 July 2022

Published: 29 July 2022

Publisher's Note: MDPI stays neutral with regard to jurisdictional claims in published maps and institutional affiliations.



Copyright: © 2022 by the authors. Licensee MDPI, Basel, Switzerland. This article is an open access article distributed under the terms and conditions of the Creative Commons Attribution (CC BY) license (<https://creativecommons.org/licenses/by/4.0/>).

1. Introduction

The diesel engine is used in a variety of fields of application, such as road transport, agricultural vehicles, earth-moving machines, rail, marine propulsion, and fixed installations for electrical power generation, due to its superior fuel economy, high torque and durability [1]. However, high nitrogen oxide (NO_x) and particulate matter (PM) emissions have led to the development of low-temperature combustion (LTC) strategies, such as homogeneous charge compression ignition (HCCI), premixed charge compression ignition (PCCI), and reactivity controlled compression ignition (RCCI) which emit less NO_x and PM because of lower flame temperature and lean combustion, respectively [2].

Dual fuel (DF) combustion is a potential alternative to these combustion technologies as it requires minimal engine modifications. DF combustion involves the use of two fuels: the first with a high octane number (primary fuel), which is injected in the intake manifold,

and the second with a lower octane number (secondary fuel, usually diesel fuel), which is injected just before the top dead center (TDC) to act as a source of ignition for the propagation of multiple flame fronts which burn the air-primary fuel mixture [3].

In recent years, research has focused on the study of DF combustion with natural gas (NG) used as the primary fuel [4–6]. The low C/H ratio of NG results in less CO₂ emissions compared to an engine that works in full diesel mode. Moreover, the lean NG/air lean mixture leads to a decrease in the maximum temperatures and, consequently, of NO_x emissions. At the same time, large quantities of carbon monoxide (CO) and unburned hydrocarbons (UHC) are produced since the equivalence ratio falls outside flammability limits, preventing efficient propagation of the flame front [7,8].

The use of gaseous hydrogen as a primary fuel provides more significant advantages in terms of emissions since hydrogen is a carbon-free fuel. Furthermore, the high low heating value and laminar flame speed result in improved thermal efficiency and a faster combustion process [9]. However, the higher adiabatic flame temperature of hydrogen compared to other fossil fuels results in large emissions of nitrogen oxides [10].

The use of hydrogen causes a decrease in volumetric efficiency as a result of the low density of hydrogen, which leads to the displacement of greater volumes of air with increasing hydrogen [11], and a strong tendency to knocking (autoignition of hydrogen before the ignition of the diesel fuel) that occurs particularly with large hydrogen energy contributions, and with high loads and compression ratios [12]. One of the biggest problems in the use of hydrogen is the high production cost. Therefore, researchers have focused on the use of hydrogen–methane mixtures as a primary fuel in DF engines to combine the advantages of the two fuels. Experimental studies [13–15] have demonstrated that blends with a higher quantity of hydrogen lead to a major peak in pressure, enhanced diesel fuel combustion (due to an advanced start to the combustion), and reduced combustion duration of the gaseous fuel phase (due to the rapid combustion speed and wider combustion limits of hydrogen). Furthermore, the use of large hydrogen proportions has been shown to be effective in lowering carbon emissions, while NO_x emissions sharply increase.

The study of combustion as the fuel used varies is of fundamental importance. A correct understanding of combustion phenomena can be achieved using a numerical three-dimensional approach. CFD 3D techniques are widely used since they provide an accurate description of the chemical and physical processes which occur in the combustion chamber and a detailed description of the flow field. Interest in this topic is demonstrated by various reports available in the scientific literature for the use of both DF methane [16–19] and hydrogen [20,21]. However, the main challenge in numerical simulations concerns the combustion model, since it needs to take into account both the combustion and the interaction of the primary with the secondary fuel. Most of the studies available use a reduced kinetic mechanism which involves a diesel surrogate (typically n-heptane or n-dodecane), methane and hydrogen [22–25].

In alignment with current research, the authors sought to investigate the modeling of the combustion of a dual fuel diesel engine, with a particular emphasis on the propagation of the flame front and evaluation of the laminar flame speed (LFS). To simulate the combustion process, a kinetic mechanism was created by merging GRIMECH 3.0 with a detailed scheme proposed by Ra and Reitz [26] for n-dodecane, used as a surrogate for diesel fuel. The mechanism, containing 124 species and 660 reactions, coupled with an autoignition-induced flame propagation model, was implemented in ANSYS Forte[®] code. The model was shown to be reliable for describing dual fuel combustion in a previous paper [27]. Using the GRIMECH 3.0 mechanism in ANSYS Chemkin-Pro, tables with values for laminar flame speed as a function of pressure, temperature and equivalence ratio were obtained. The accuracy of this approach was verified by comparing the trend in the laminar flame speed derived from tables with the LFS obtained using well-established correlations. The approach described represents a valuable method for modeling dual-fuel combustion phenomena.

Since the authors have focused extensively on DF operation with methane in a single cylinder research engine in previous experimental and numerical work [28–31], this paper

mainly seeks to highlight differences in the use of hydrogen as a primary fuel compared to methane for the same research engine. In particular, an analysis was conducted by comparing the experimental results with methane and hydrogen and then by comparing the numerical 3D CFD results obtained for different test cases with hydrogen, methane and hydrogen-methane mixtures, with the same total energy input, but varying the energy provided by hydrogen (i.e., 0, 25, 50, 75 and 100%). In the simulations performed, the focus was on the development of the combustion process and evaluation of chemical species trends, including pollutant emissions, by testing the goodness of fit of the combustion model used.

2. Experimental Test Cases

The experiments were performed on a research single-cylinder diesel engine in dual fuel mode as described in previous papers [28–31].

The engine (Table 1) was equipped with a common rail injection system and the cylinder head of a real four-cylinder diesel engine. Valve timings were fixed for all tests; their values are listed in Table 2. Diesel injection was achieved with the use of a seven-hole-injector, and was controlled by an electronic control unit (ECU). The methane or hydrogen gaseous fuel was injected in the intake manifold using a commercial gas PFI electro-injector with a maximum pressure of injection of 5 bar. The port fuel injection was controlled by a delay unit synchronized with the engine shaft encoder. The injection system specifications are summarized in Table 3.

Table 1. Engine specifications.

Engine Type	Stroke [mm]	Bore [mm]	Cylinder Volume [cm ³]	Bowl [cm ³]	Compression Ratio
4-stroke single-cylinder 4 valves	92	85	522	19.7	16.5:1

Table 2. Opening and closing valve timing.

EVO	EVC	IVO	IVC
116° ATDC	340° BTDC	344° ATDC	132° BTDC

Table 3. Injection system specifications.

Diesel Injection System	Number of Holes	Cone Angle Axis [deg]	Hole Diameter [mm]	H ₂ /CH ₄ Injection System	Holes Number of H ₂ /CH ₄ Injector	Maximum PFI Pressure [bar]
Common Rail	7	148	0.141	PFI	1	5

A piezoelectric pressure sensor installed in the cylinder head, in place of a preheating glow plug, alongside a multichannel acquisition system, enabled measurement of the pressure cycles. The experimental in-cylinder pressure cycles were taken as benchmarks to represent the average cycle over 200 cycles, assuming the uncertainty of the measurements to be equal to ±0.5 bar.

The test cases involved dual-fuel operation, varying the premixed fuel (natural gas or hydrogen); the engine operating conditions are listed in Tables 4 and 5.

The initiation of the pilot and main injections (SOI) was dependent on the current signal, so a mechanical delay (about 300 μs) was needed for opening of the nozzle. Experimental measurements of the fuel and air mass flow rates taken enabled calculation of the thermal energy provided by the fuels, the equivalence ratio and premixed ratio (*RP*).

$$RP = \frac{(m_p LHV_p)}{(m_p LHV_p + m_d LHV_d)} \times 100 \quad (1)$$

where m_p and m_d are the mass flow rate of the premixed fuel (methane or hydrogen) and the directly injected fuel (diesel), respectively, and LHV_p and LHV_d are their low heating values.

Table 4. Engine operating conditions for the cases with methane.

	M1	M2	M3	M4
Engine speed [rpm]	1500	1500	2000	2000
IMEP [bar]	1.9	4.8	2	4.3
Pilot SOI [deg]	−16	−11.6	−21.2	−18.6
Main SOI [deg]	−6	0.3	−8	−2.4
Dwell [deg]	10	11.9	13.2	16.2
Rail pressure [bar]	615	867	700	891
Pilot and main duration [deg]	2.6	2.4	3.4	3.1
Pilot and main diesel mass injected [mg/cycle]	0.711	0.822	0.717	0.833
Thermal energy from diesel [J]	61.15	70.69	61.66	71.64
Methane mass [mg/cycle]	7.58	11.19	7.55	10.15
Thermal energy from methane [J]	379	559.5	377.5	507.5
Total thermal energy from fuels [J]	440.15	630.19	439.16	579.16
Inlet pressure [bar]	1.5	1.7	1.5	1.7
Inlet temperature [°C]	44	46	50	51
Air mass [mg/cycle]	750.9	802.4	679.3	741.2
Methane/air ER	0.174	0.240	0.192	0.236
RP [%]	86.10	88.78	85.97	87.62

Table 5. Engine operating conditions for the test cases with hydrogen.

	H1	H2	H3	H4
Engine speed [rpm]	1500	1500	2000	2000
IMEP [bar]	0.9	3	0.9	2.7
Pilot SOI [deg]	−16	−11.6	−21.2	−18.6
Main SOI [deg]	−6	0.3	−8	−2.4
Dwell [deg]	10	11.9	13.2	16.2
Rail pressure [bar]	615	867	700	891
Pilot and main duration [deg]	2.6	2.4	3.4	3.1
Pilot and main diesel mass injected [mg/cycle]	0.711	0.822	0.717	0.833
Thermal energy from diesel [J]	61.15	70.69	61.66	71.64
Hydrogen mass [mg/cycle]	2.45	4.35	2.32	3.92
Thermal energy from hydrogen [J]	295	523	279	470
Total thermal energy from fuels [J]	356.15	593.69	340.66	541.64
Inlet pressure [bar]	1.5	1.7	1.5	1.7
Inlet temperature [°C]	44	51	55	59
Air mass [mg/cycle]	727.5	796	672	738.6
Hydrogen/air ER	0.115	0.187	0.118	0.181
RP [%]	82.8	88.1	81.9	86.8

It is worth noting that the tests were characterized by similarly low values of the equivalence ratio (ranging from 0.115 to 0.240) and of the premixed ratio (above 81%). In particular, the high RP values in Table 4 indicated that most of the energy supply was provided by the primary fuel (methane or hydrogen). Figures 1–6 display the experimental in-cylinder pressure, the rate of heat release and the accumulated heat release for methane and hydrogen. The curves in the diagrams corresponding to the experimental cases with the same diesel mass flow and injection timings (SOI and duration of pilot and main injections) have the same color.

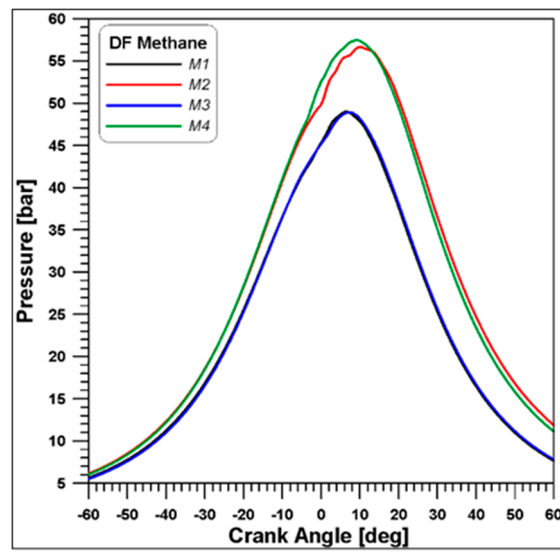


Figure 1. Experimental in-cylinder pressure. Cases with methane.

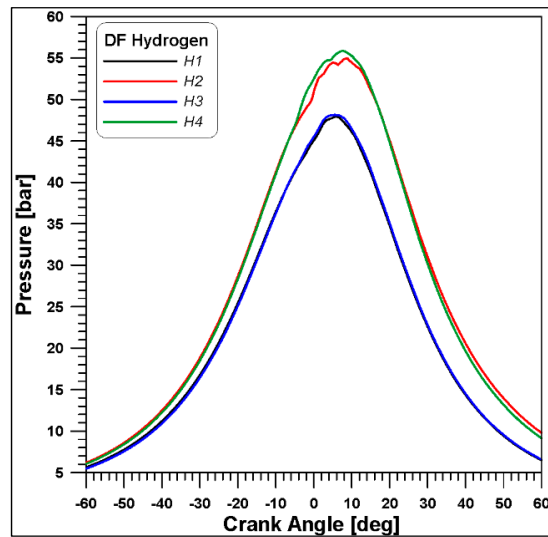


Figure 2. Experimental in-cylinder pressure. Cases with hydrogen.

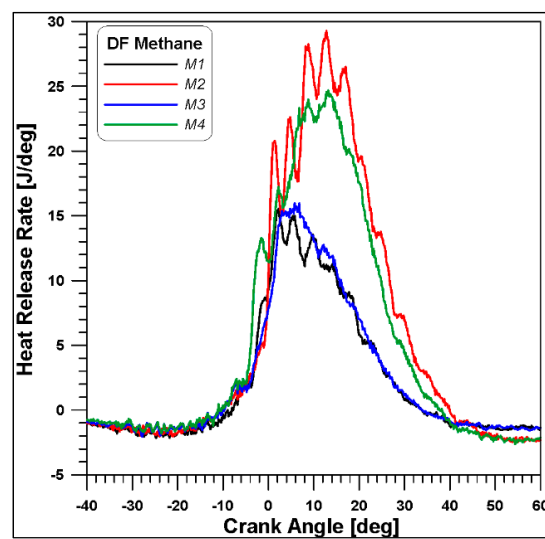


Figure 3. Experimental heat release rate. Cases with methane.

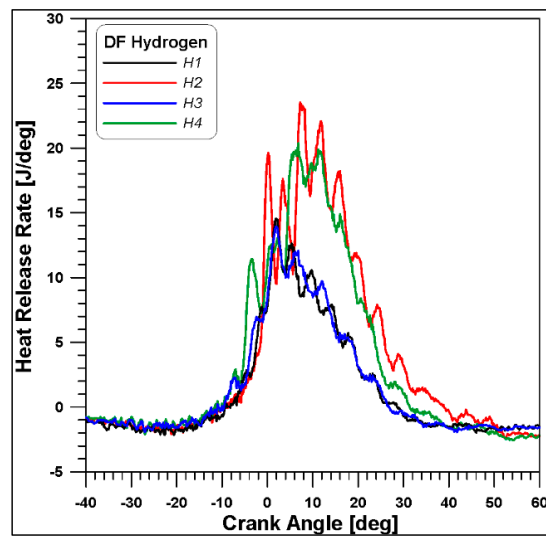


Figure 4. Experimental heat release rate. Cases with hydrogen.

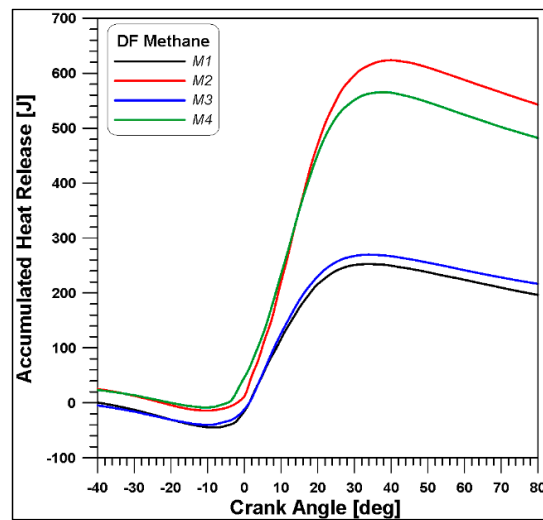


Figure 5. Accumulated heat release. Cases with methane.

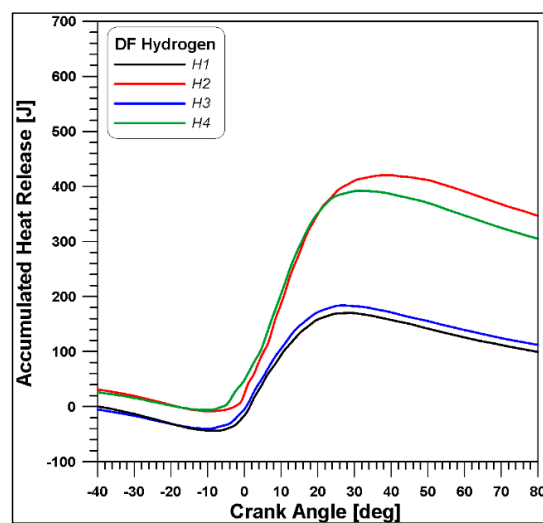


Figure 6. Accumulated heat release. Cases with hydrogen.

Similar considerations apply to both fuels, whose curves present the same trends. The pressure graphs (Figures 1 and 2) show that the difference in the pressure peak was mainly due to the different IMEP values (the red and green curves are at a higher load). However, the engine speed also affected the pressure, since higher speeds (blue and green curves are at 2000 rpm) led to higher peaks of pressure for similar IMEP values.

The rate of heat release shown in Figures 3 and 4 reflects typical dual-fuel combustion behavior: in the first part of the combustion process, only a small amount of the pilot diesel fuel burns and this enables control of the ignition timing of the air-fuel mixture that occurs when the main diesel injection is provided. However, when the pilot injection occurs long in advance, and the energy provided by the primary fuel is sufficiently high, the pilot fuel causes the ignition of a part of the methane–air or hydrogen–air mixture (green curves). Furthermore, the heat release rate indicates that the higher energy contribution provided by the primary fuel led to a more rapid and intense combustion (greater slope of the green curves at 5° BTDC and higher heat release rate peaks).

The accumulated heat release rate diagrams (Figures 5 and 6) confirm this trend, showing how cases with higher energy inputs correspond to the major final values of the total energy.

Finally, a comparison between the case M3 (methane) and H4 (hydrogen) is reported in Figure 7. These two cases are taken as the basis for a first comparison since they have the same engine speed, and the values of the equivalence ratio and RP are very similar. For a better comparison, the graph of the heat release rate is normalized with respect to the total fuel energy.

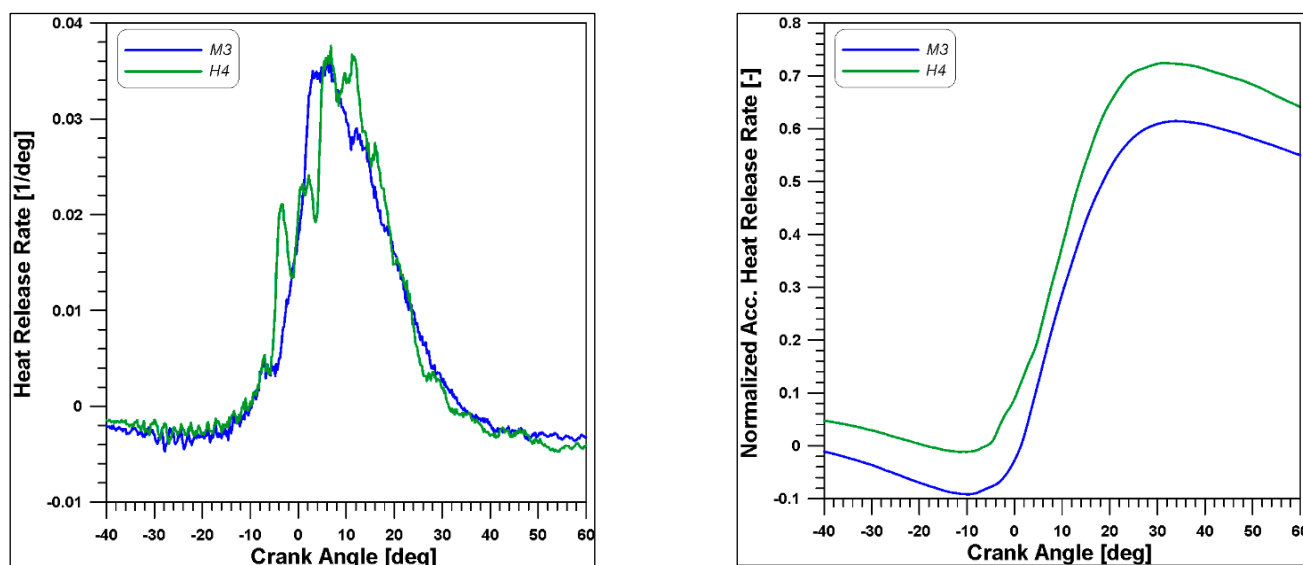


Figure 7. Comparison of normalized heat release rate and accumulated heat release (M3 vs. H4).

It was observed that the ignition of the pilot diesel fuel occurred at about the same crank angle although the injection of diesel fuel occurred later for the H4 case (SOI pilot of -21.2° for M3 vs. SOI pilot of -18.6° for H4). Thus, the presence of hydrogen accelerated the diesel combustion reactions. Consequently, the pilot injection was sufficient to burn part of the hydrogen–air mixture whereas the main injection was necessary for the combustion of the methane. Moreover, the hydrogen combustion appeared faster since the slope of the curve was greater.

A further comparison between the M2 and H2 cases (Figure 8) confirmed that, even when the energy inputs were similar (559.5 J of methane potential thermal energy vs. 523 J of hydrogen potential thermal energy), the ignition of hydrogen occurred in advance, confirming its higher reactivity.

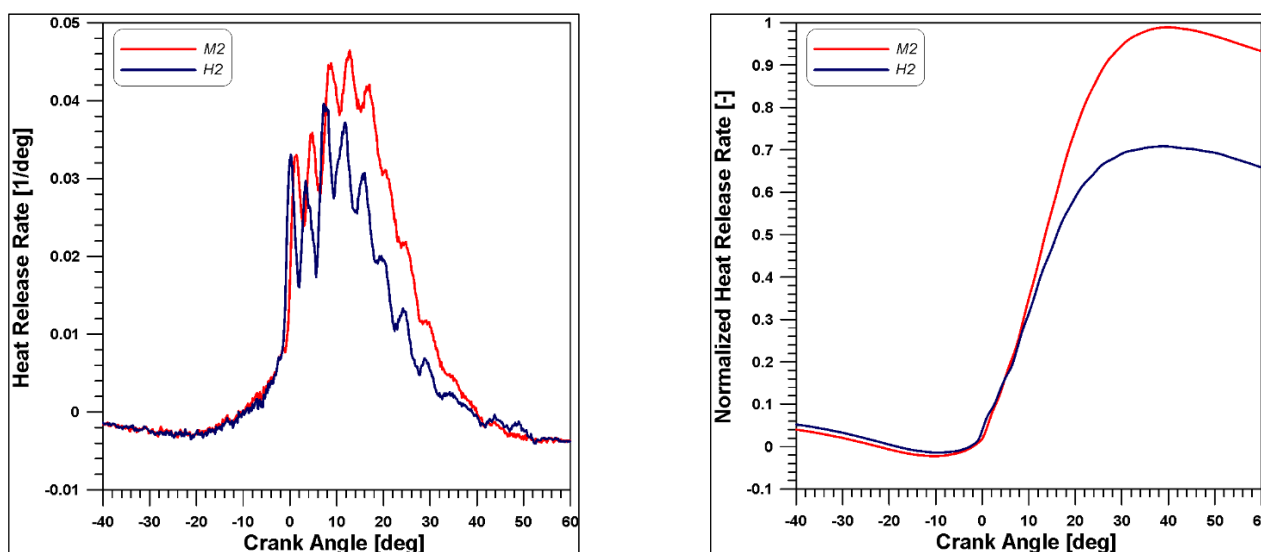


Figure 8. Comparison of normalized heat release rates and accumulated heat release (M3 vs. H4).

3. Combustion Modeling

3.1. Methodology

As explained in Section 1, the authors constructed a kinetic mechanism model based on GRIMECH 3.0 with a detailed scheme proposed by Ra and Reitz [26] for n-dodecane as a surrogate for diesel fuel. The mechanism, containing 124 species and 660 reactions, coupled with an autoignition-induced flame propagation model, was implemented in ANSYS Forte[®] code as described in previous papers [27,28]. The initiation of flame propagation induced by the autoignition kinetics was represented by the oxidation and the relative reaction scheme for n-dodecane, while the autoignition-induced flame propagation measurements were used by the software to track the position of the flame front. Using the GRIMECH 3.0 mechanism in ANSYS Chemkin-Pro, tables with values of laminar flame speed (LFS) as a function of conditions of pressure, temperature and equivalence ratio were obtained. The tables were used by ANSYS Forte[®] to evaluate the laminar flame speed values by interpolation. The accuracy of this approach was verified by comparing the trend in the laminar flame speed derived from tables with the LFS obtained with the use of LFS correlations. The RANS RNG k- ϵ model was used to simulate the turbulence. Finally, for the diesel spray simulation, the KHRT atomization model and a discrete multi-component (DMC) fuel vaporization model were used. For study of the combustion process, the simulations described below were performed with closed valves.

3.2. Mesh Sensitivity Analysis

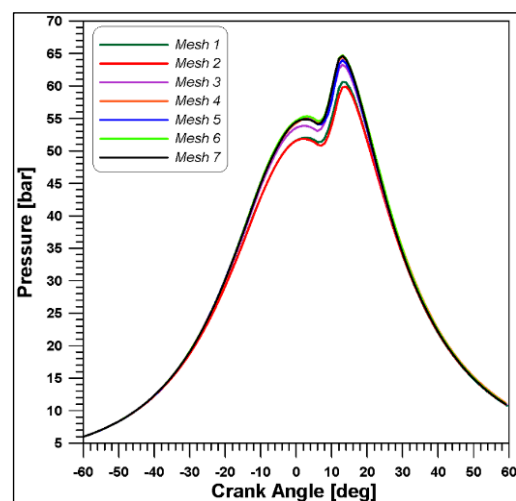
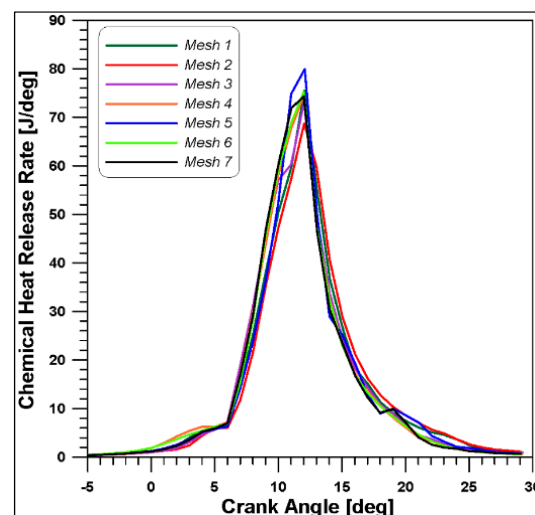
The meshes and calculations were carried out on a sector angle of the engine of 51.43°. The number of cells and the average size of the tetrahedral cells of the meshes at TDC are reported in Table 6. With the aim of identifying the mesh which provided the best compromise between computational time and solution accuracy, for each mesh, a simulation in full diesel mode was performed using the settings reported in Table 7. The mesh sensitivity analysis was performed by comparing trends of the in-cylinder pressure and chemical heat release (Figures 9 and 10). To better understand the in-cylinder pressure difference, in Figure 11 the evolution of the mass inside the cylinder is reported. It is possible to notice that, in the coarse meshes, the lost mass through the crevices was greater during the compression phase, while, during the expansion phase, the mass returned more quickly. Moreover, when the mesh was not sufficiently fine, the vaporization and atomization phenomena were not well described, with consequent lower pressure during the combustion. Although the meshes 4, 6 and 7 each provided the most accurate results, mesh 4 (Figure 12) was chosen because it involved reduced computational time.

Table 6. Mesh characteristics.

#Mesh	Average Size of Cells at TDC [mm]	Number of Cells at TDC
1	0.730	12,516
2	0.543	30,336
3	0.535	31,776
4	0.514	35,748
5	0.486	42,368
6	0.424	63,693
7	0.401	75,488

Table 7. Simulation settings for the full diesel simulations.

Parameter	Data
Engine speed [rpm]	2000
SOI pilot [deg]	15° BTDC
SOI main [deg]	1.2° ATDC
Duration of pilot injection [deg]	7
Duration of main injection [deg]	10
Pilot and main diesel mass [mg/cycle]	12

**Figure 9.** Pressure for the different meshes.**Figure 10.** Rate of heat release for the different meshes.

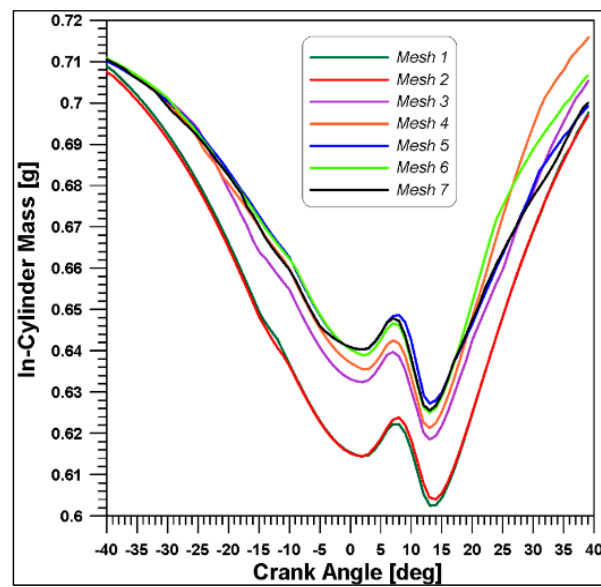


Figure 11. Mass inside the cylinder.

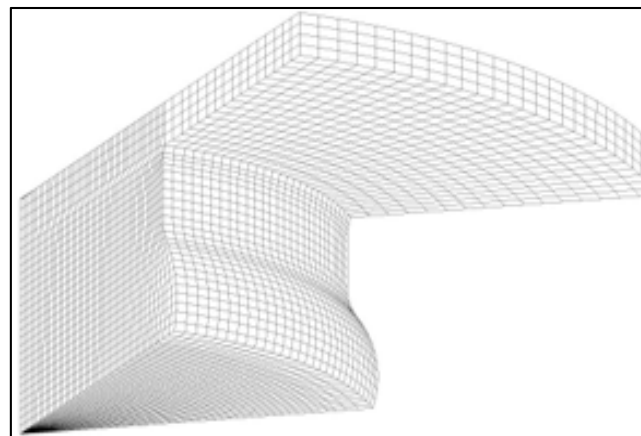


Figure 12. Mesh#4.

3.3. Model Tuning

Validation of the model was performed by simulating the test case H4 (see Table 5), reproducing the same experimental operating conditions. Several simulations were carried out by varying certain model parameters and empirical constants. All the simulations were conducted with closed valves (from 132° BTDC to 116° ATDC); the pilot and main SOI were 15° BTDC and 1.2° ATDC, respectively. The simulation results reported below refer to the best tuning performed (Table 8).

Table 8. Simulation settings.

Pilot and main injection duration [deg]	3.1°
Pilot and main mass injected [mg/cycle]	0.83
Turbulent kinetic energy [cm ² /s ²]	3.42×10^4
Turbulent length scale [cm]	0.2378
Size constant of KH breakup	1
Time constant of KH breakup	40
Size constant of RT breakup	0.15
Time constant of RT breakup	1

As can be seen from the graphs of pressure and heat release (Figures 13 and 14), the numerical results matched the experimental data quite well, although there were some differences between the curves of heat release rate, since, in the numerical simulations, the combustion started slightly later than in the experiments.

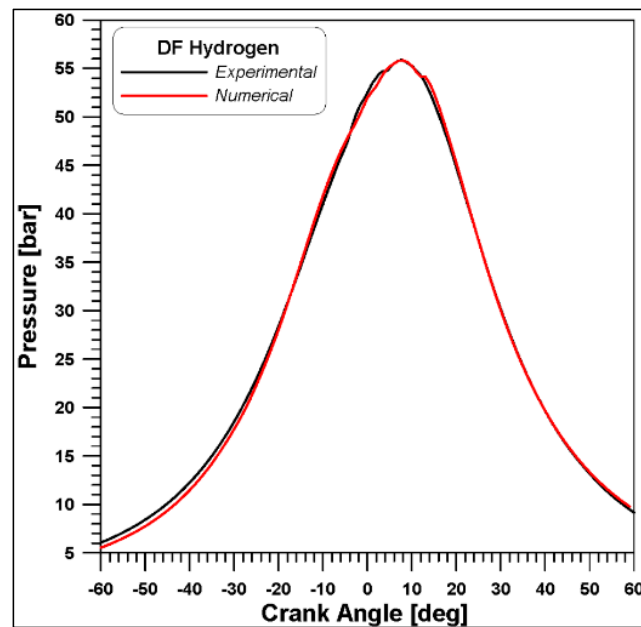


Figure 13. In-cylinder pressure. Experimental vs. Numerical.

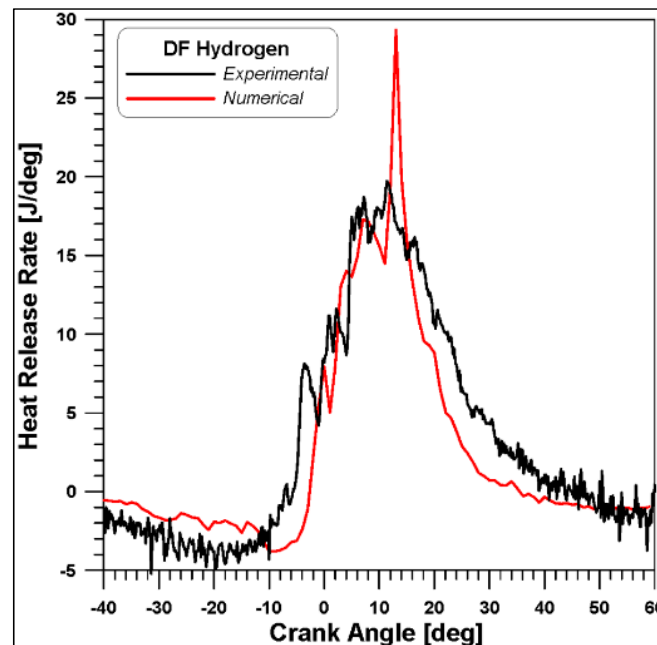


Figure 14. Rate of heat release. Experimental vs. Numerical.

Finally, Figure 15 shows that the hydrogen was not completely burned (about 35% of the hydrogen did not burn), contrary to expectations, while the diesel fuel vaporized quickly and burned entirely. The incomplete burning of hydrogen could be due to the very lean mixture used, with an equivalence ratio value of 0.2.

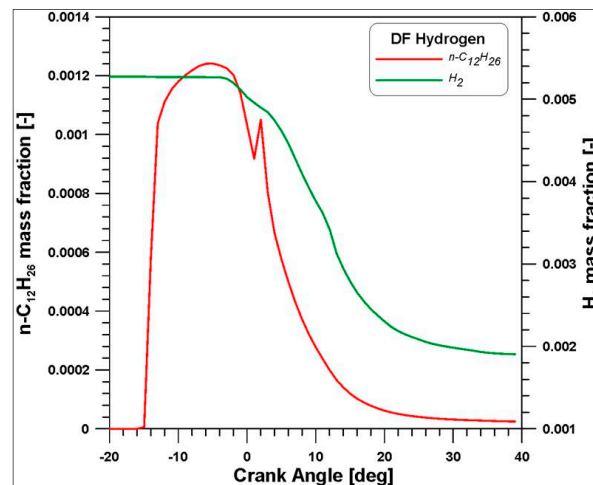


Figure 15. Numerical H_2 and $n-C_{12}H_{26}$ mass fraction.

3.4. Hydrogen-Methane Mixtures: Results and Discussion

Starting from the previous simulation with hydrogen as the gaseous fuel validated against the experimental results, several calculations were performed varying the percentage of hydrogen in the premixed mixture, while maintaining the same amount of diesel injected and the injection timing. The simulations were carried out with hydrogen–methane mixtures, always in dual-fuel mode, keeping the same fuel energy input as in the H4 case (Table 5).

In Table 9, a summary of the input mass fractions, energy and the initial conditions of pressure and temperature for each test case is reported. The test case HES100 corresponds to the previous simulation with only hydrogen as the primary fuel, while HES0 includes only methane.

Table 9. Input data for the test cases.

	HES100	HES75	HES50	HES25	HES0
E_{H_2} [J]	470	352.5	235	2.27	0
E_{CH_4} [J]	0	117.5	235	2.60	470
m_{H_2} [mg]	3.92	2.94	1.96	0.98	0
m_{CH_4} [mg]	0	2.35	4.70	7.05	9.4
x_{H_2}	0.00527	0.00395	0.00263	0.00131	0
x_{CH_4}	0	0.00316	0.00631	0.00944	0.01256
Initial pressure [bar]	1.591	1.591	1.591	1.591	1.591
Initial temperature [K]	346.4	346.4	346.4	346.4	346.4
Mass [mg]	742.6	753.2	764.2	775.4	786.9
Gaseous fuel/airER	0.184	0.203	0.212	0.221	0.184
RP [%]	86.8	86.8	86.8	86.8	86.8

The in-cylinder pressures (Figure 16) show that, for reduced hydrogen content, a lower pressure peak was observed. This was probably due to the slower reactivity of methane at high temperatures compared to that of hydrogen. Furthermore, by reducing the hydrogen share, a second peak became evident since only the pilot diesel fuel burned before TDC, while the mixture started to burn when the main injection occurred.

The curves of the rate of heat release confirmed this phenomenon (Figure 17): in the case with only hydrogen (HES100), an earlier combustion start occurred, and the mixture reacted more actively. In the HES0 case (only methane), the pilot injection did not initiate the premixed combustion. The consequence was a sharp increase following the main injection (SOI 1.2° ATDC) since a large part of the methane present burned simultaneously. The HES50 case, as expected, showed intermediate behavior between the two extreme cases of HES100 and HES0.

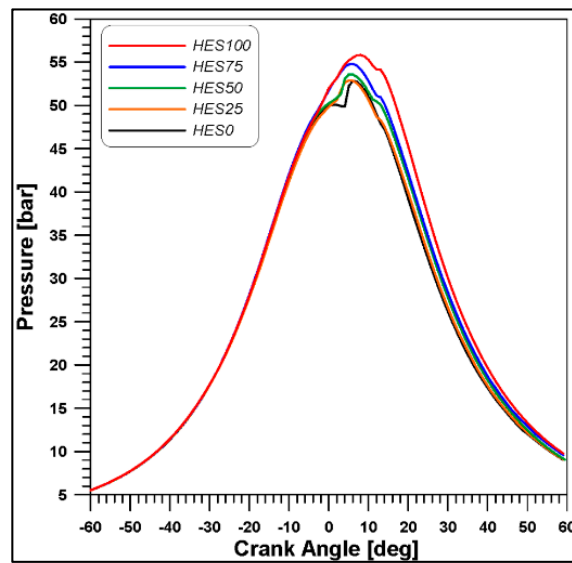


Figure 16. In-cylinder pressures.

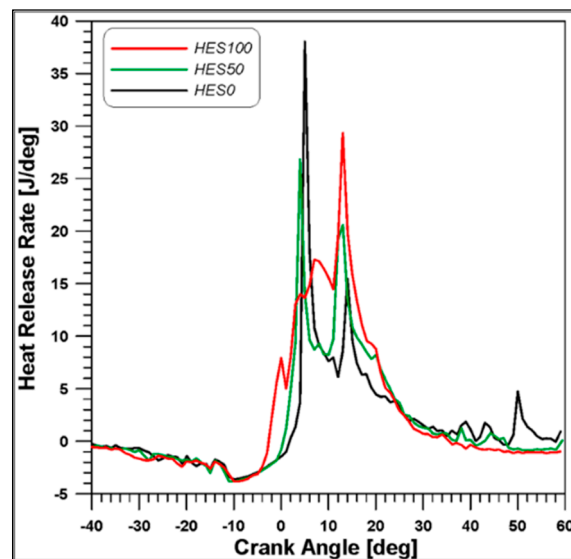


Figure 17. Rate of heat release.

The accumulated heat release in Figure 18 highlights that the combustion was not completed when the input energy value was not reached (see Table 9). Furthermore, for the HES25 and HES0 cases, the heat release increased constantly up to 80° ATDC.

The evolution of the gaseous fuel mass fraction (hydrogen and methane) shown in Figure 19 indicates that the fastest fuel consumption occurred in the HES100 case. The same figure provides additional evidence that the initiation of combustion of pure hydrogen occurred close to the pilot injection event. In the HES0 case (pure methane in the premixed mixture), the combustion of gaseous fuel was clearly activated by the main injection.

On the other hand, Figure 20 shows that a large amount of diesel fuel vapor was still present with increasing methane content. Following the main injection, more fuel vapor remained because it could not oxidize. The temperature values provide an explanation: the reduced amount of hydrogen, and, at the same time, the increase in methane, led to lower temperatures peaks (Figure 21) and the maximum temperature zones were less extensive, as shown in Figure 22, slowing the fuel oxidation. For all cases, it was observed that the high temperature zones were concentrated in the center of the combustion chamber.

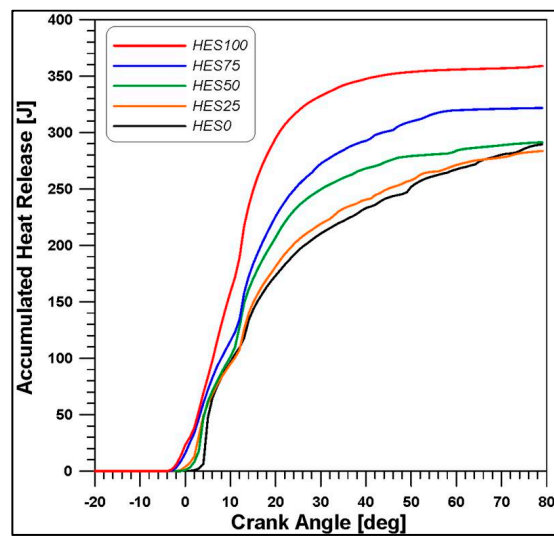


Figure 18. Accumulated chemical heat release.

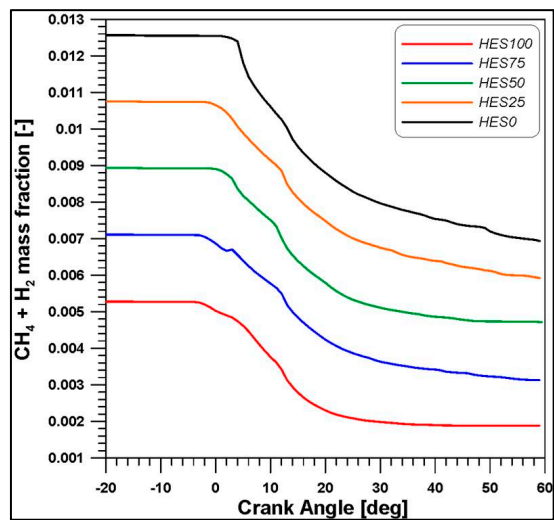
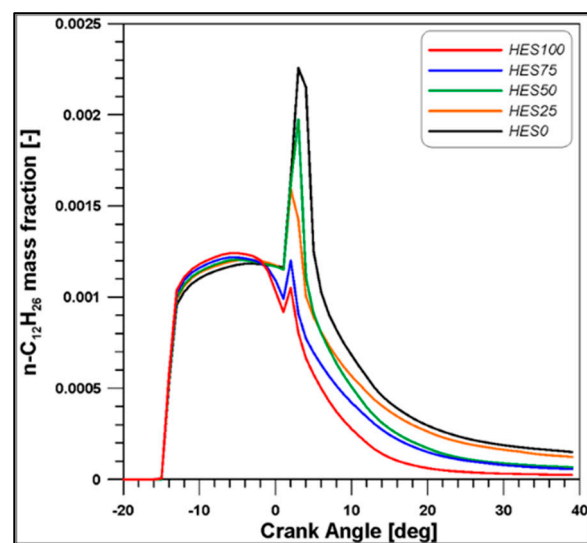
Figure 19. Fuel (H₂ + CH₄) mass fraction.

Figure 20. Diesel mass fraction.

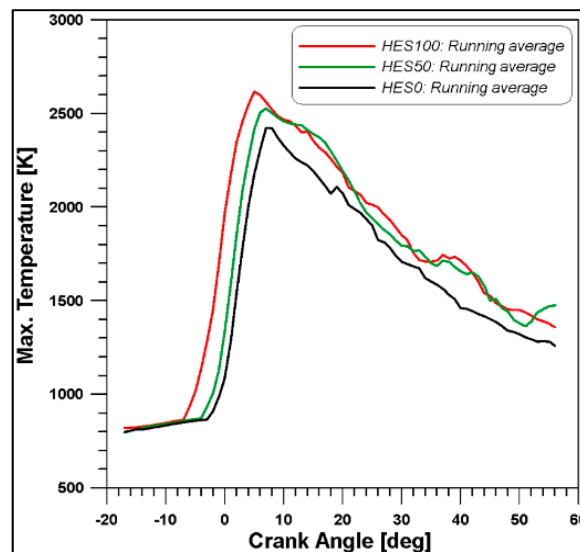


Figure 21. Maximum temperatures.

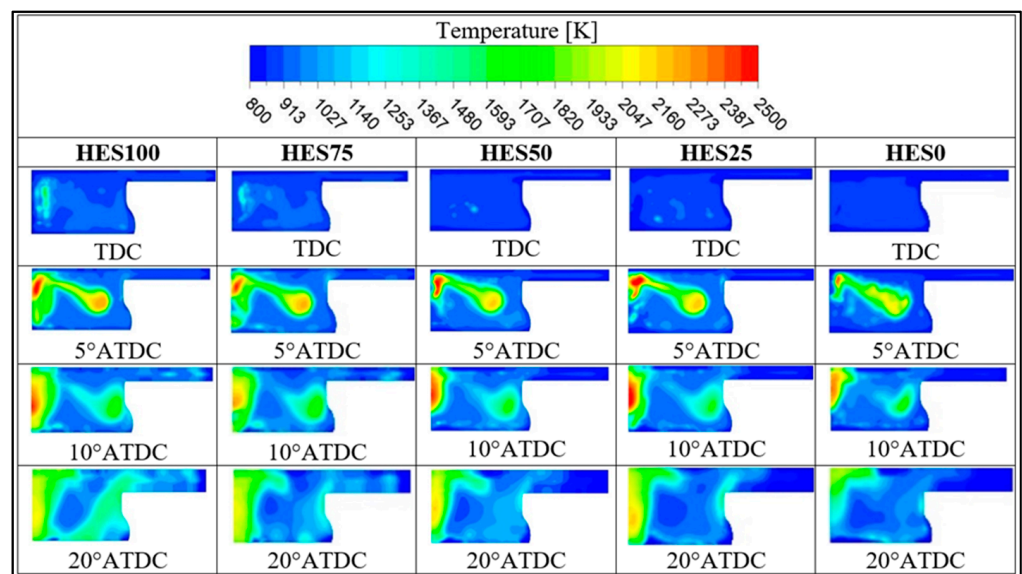


Figure 22. Temperature distributions for the different HES cases.

By examining the hydrogen contours in Figure 23, the locations of the mixture consumption can be identified; comparing the HES100 and HES0 cases, the hydrogen tended to burn even at a distance from the areas with the major concentration of diesel vapor (Figure 24). In this regard, it is useful to examine the development of the flame and, therefore, the ‘G’ function, which describes the flame propagation, as represented in Figure 25. The regions where $G > 0$ correspond to the zones where the premixed charge was being consumed, the zones where $G < 0$ identify the unburned mixture, while the flame front is localized where the function assumes a value $G = 0$. From this analysis, it is evident that the hydrogen combustion began early and that the flame spread more in the combustion chamber at TDC for the HES100 case, continuing its development at the following crank angles. In the case of HES0, the flame had not even started to propagate at TDC, in confirmation of the previous results.

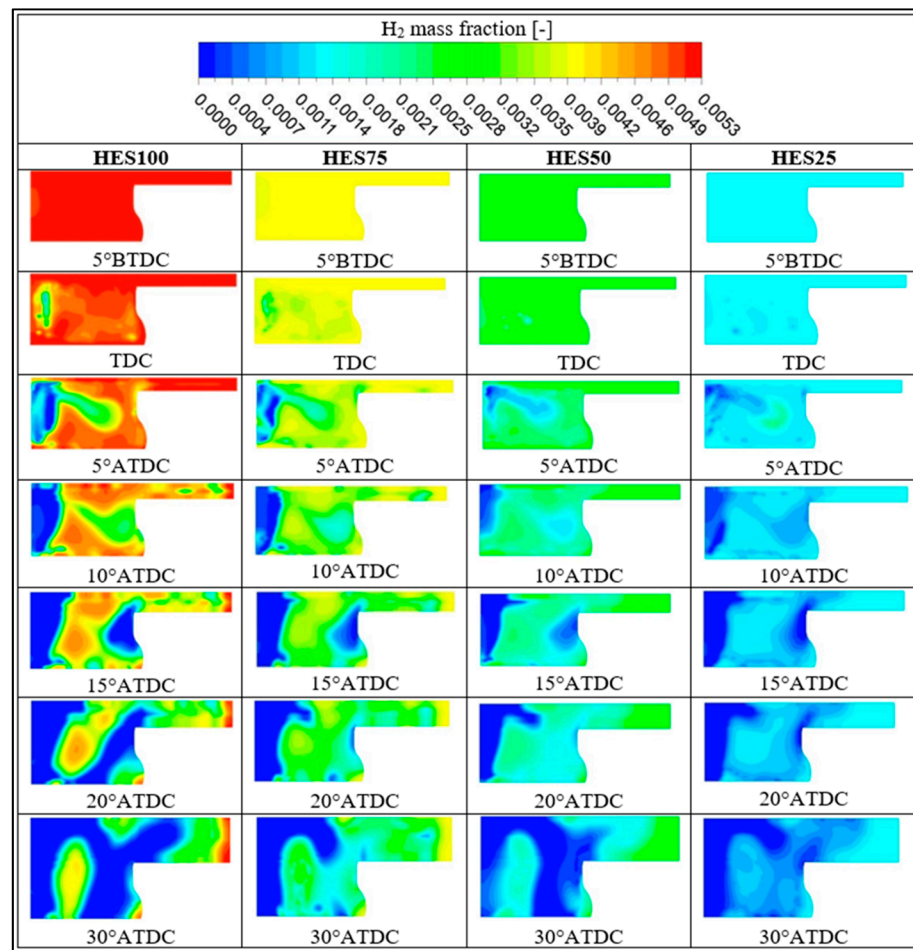


Figure 23. Hydrogen mass fraction distributions for the different HES cases.

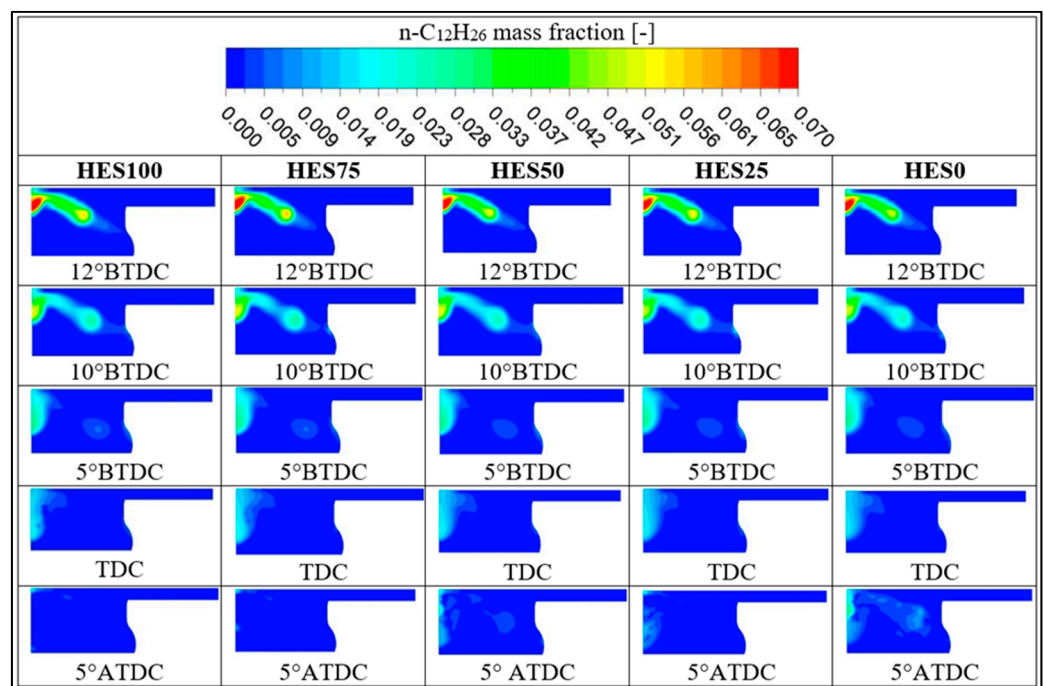


Figure 24. Diesel mass fraction distributions for the different HES cases.

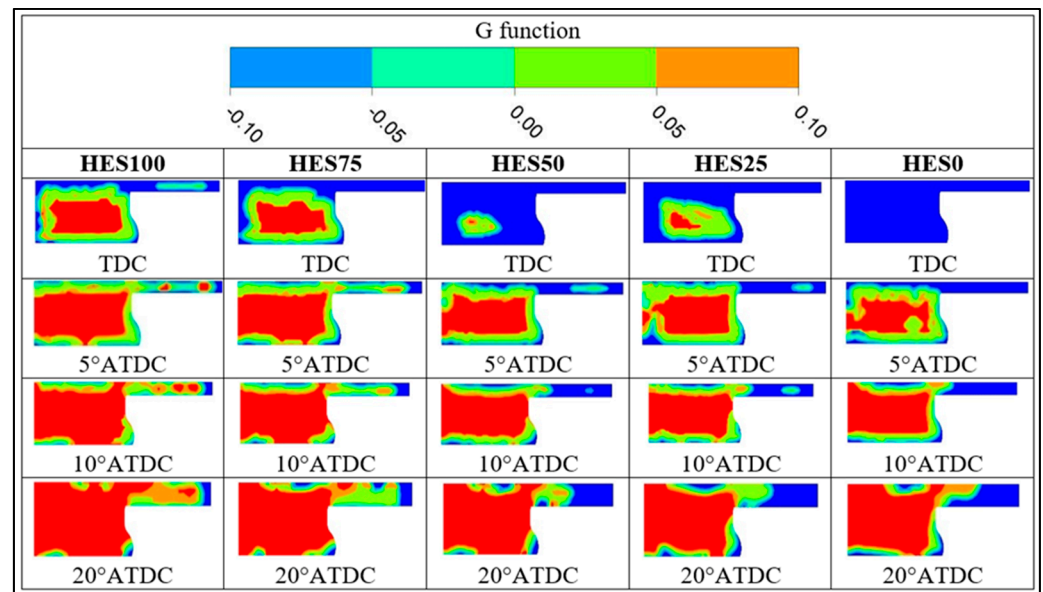


Figure 25. G function distributions for the different HES cases.

For completeness, the laminar and turbulent flame speed trends are shown in Figure 26. Only three cases (HES0, HES50, HES100) are plotted for a more readable representation. For each case, the trends of the laminar and turbulent speeds were almost the same, with higher values for the second speed, especially in the first part, confirmed by the high turbulent kinetic energy values (Figure 27). Both speeds reached higher values by increasing the hydrogen presence in the mixture, in addition to the fact that the flame propagation in the mixture started earlier, as already verified. It should be remembered that the curves in Figure 26 display the trend in the in-cylinder averaged flame speed. In fact, multiple flame fronts were generated by the diesel fuel jets. Nevertheless, the G function contours in Figure 25 clearly demonstrate that the peripheral zones inside the cylinder were not yet reached by the flame front at 20° ATDC.

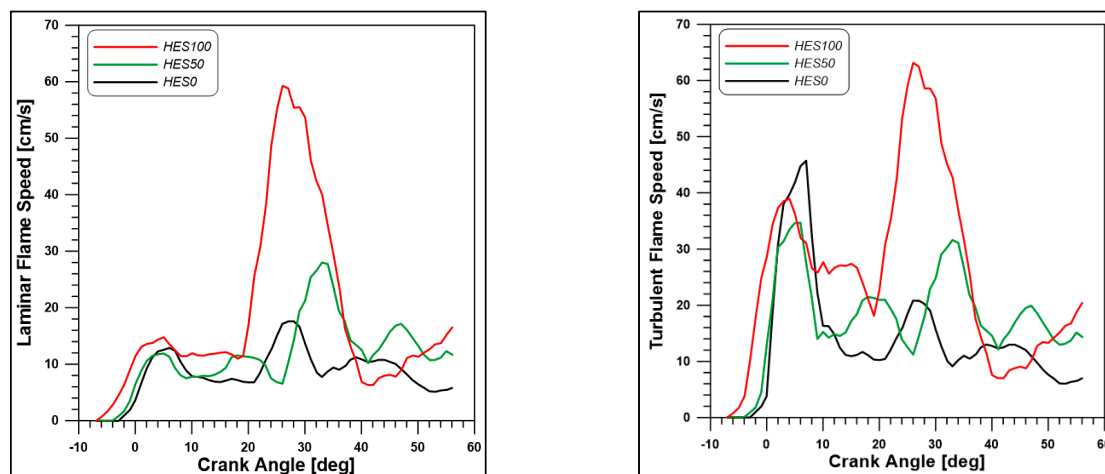


Figure 26. Laminar and turbulent flame speeds.

In Tables 10 and 11, a summary of the results is reported. The HES100 case indicates higher work (in terms of IMEP, calculated at closed valves) and power because of the better thermal and combustion efficiency. Moreover, the HES100 case involved faster combustion of lower duration (HRR10-HRR90). The results were very similar in the first half of the combustion process (from HRR10 to HRR50), while, in the second part (from HRR50 to

HRR90), the progressive replacement of hydrogen with methane led to slowing of this phase. The final values (at EVO) of the concentration of some of the most important chemical species are displayed in Table 11.

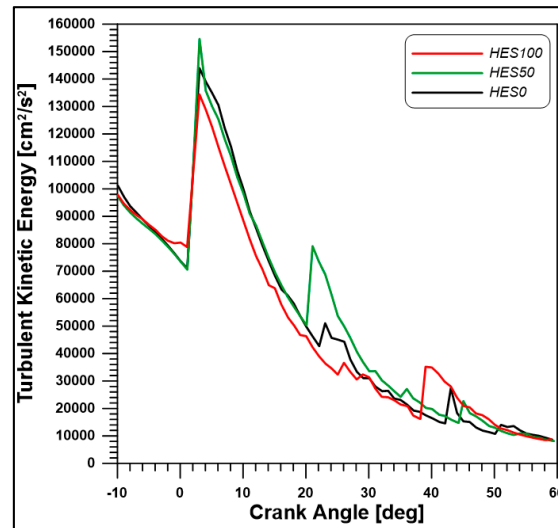


Figure 27. Turbulent kinetic energy.

Table 10. Engine summary for the different HES cases.

	HES100	HES75	HES50	HES25	HES0
Gross power [kW]	2.61	2.27	2.07	2.07	1.88
IMEP [bar]	3.0	2.60	2.38	2.21	2.16
Combustion efficiency	0.66	0.60	0.56	0.56	0.58
Thermal efficiency	0.29	0.25	0.24	0.24	0.22
Total chemical heat release [J]	361	323	294	294	296
Total wall heat transfer loss [J]	52	47	45	45	42
Total net heat [J]	309	276	249	249	254
Total net heat (from PV with variable Gamma) [J]	215	186	165	165	168
Max. pressure [bar]	55.8	54.8	53.4	53.4	52.8
Max. temperature [K]	1179	1066	1035	1035	983
Max. pressure rise rate [bar/deg]	1.44	1.44	1.74	1.74	2.36
HRR10 [deg ATDC]	2	2	4	4	5
HRR50 [deg ATDC]	12	14	13	13	16
HRR90 [deg ATDC]	27	39	38	38	60
HRR10-HRR90 Duration [deg]	25	37	34	34	55

Table 11. Final concentrations of some chemical species.

	HES100	HES75	HES50	HES25	HES0
H ₂	1877	1731	1342	690	0
CH ₄	0	1403	3244	4984	6404
n-C ₁₂ H ₂₆	18.30	33.98	45.65	66.42	78.58
CO ₂	32,648	28,082	24,590	21,502	17,649
O ₂	193,871	196,419	198,408	197,990	195,845
CO	226	569	818	888	860
NO _x	2.66	2.16	1.50	1.96	0.45

The HC emissions (Figure 28) showed higher values by reducing H₂ in the mixture, also considering that, in the HES100 case, the only carbon atoms present were due to the diesel fuel. In the other test cases, the higher unburned hydrocarbon value was also due to unburned methane. The higher temperatures caused high NO_x emissions as a result (Figure 29). As expected, the introduction of hydrogen significantly reduced the production of carbon dioxide (Figure 30), as reported in many studies, e.g., [13,20,23].

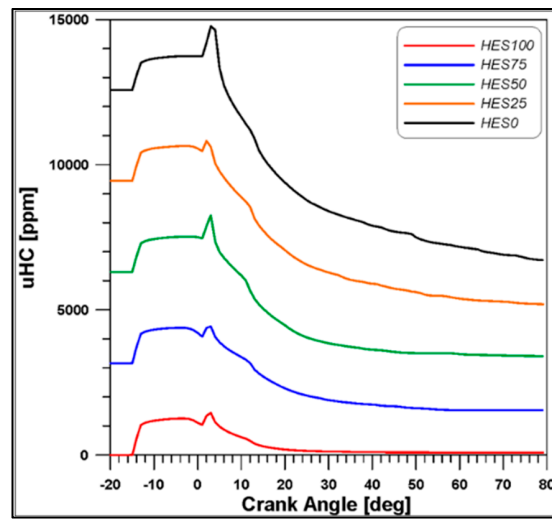


Figure 28. HC pollutant.

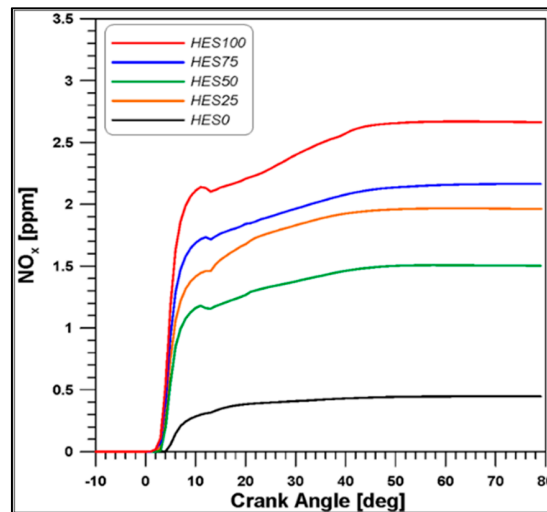


Figure 29. NO_x emissions.

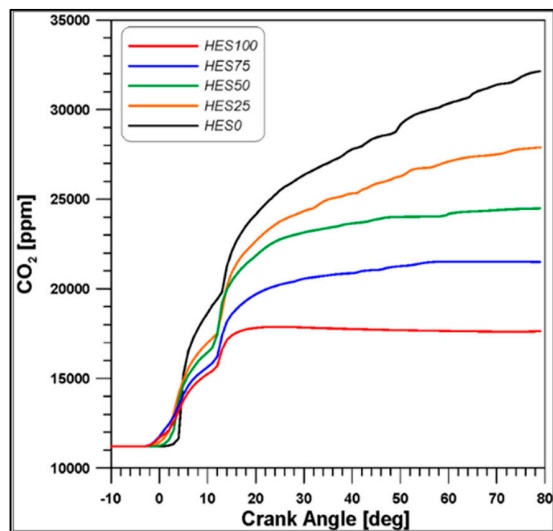


Figure 30. CO₂ emissions.

4. Conclusions

The main objective of this investigation was to numerically examine the phenomenon of dual-fuel combustion with hydrogen/methane blends used as primary fuels in a research compression ignition engine. A detailed study on combustion development was carried out to evaluate the impact of hydrogen addition on the process and emissions. After validation of the model by comparison with experimental data, several calculations were performed to estimate the effects of hydrogen in the blend on engine performance and low emissions.

The conclusions of the investigation can be summarized as follows:

- Under the operating conditions considered, the gaseous fuel did not burn completely and most of the unburned hydrogen was concentrated near the crevice region.
- The comparison between the different dual-fuel cases with the hydrogen–methane mixtures showed that the addition of methane entailed a slowing down of combustion with lower efficiency. By increasing the hydrogen amount up to 100% of the premixed fuel, the thermal and combustion efficiency increased.
- With respect to pollutant emissions, the model applied confirmed the results of previous studies, e.g., [13,20,23]: the presence of hydrogen led to less carbon-based emissions, but higher NO_x emissions due to the high temperatures.
- Future numerical studies should focus on NO_x reduction by proven EGR systems and reduce unburned hydrogen through hydrogen direct injection to avoid fuel accumulation in crevices.

Author Contributions: Conceptualization, M.C.C. and E.M.; methodology, M.C.C. and R.D.R.; software, M.P.; validation, R.D.R. and M.P.; investigation, R.D.R. and E.M.; data curation, M.P.; original draft preparation, M.C.C. and M.P.; review, R.D.R.; supervision, M.C.C. and E.M. All authors have read and agreed to the published version of the manuscript.

Funding: This research received no external funding.

Acknowledgments: Thanks to Carlo Rossi of STEMS Institute of Naples for the support provided for the experimentation. The calculations are licensed by ANSYS®.

Conflicts of Interest: The authors declare no conflict of interest.

References

1. Heywood, J.B. *Internal Combustion Engines Fundamentals*; McGraw-Hill: Grapeport, OH, USA, 2018.
2. Krishnamoorthi, M.; Malayalamurthi, R.; He, Z.; Kandasamy, S. A review on low temperature combustion engines: Performance, combustion and emission characteristics. *Renew. Sustain. Energy Rev.* **2019**, *116*, 109404. [[CrossRef](#)]
3. Pham, Q.; Park, S.; Agarwal, A.K.; Park, S. Review of dual-fuel combustion in the compression-ignition engine: Spray, combustion, and emission. *Energy* **2022**, *250*, 123778. [[CrossRef](#)]
4. Zhang, W.; Feng, T.; Li, Z.; Chen, Z.; Zhao, J. EGR thermal and chemical effects on combustion and emission of diesel/natural gas dual-fuel engine. *Fuel* **2021**, *302*, 121161. [[CrossRef](#)]
5. Xu, M.; Cheng, W.; Zhang, H.; An, T.; Zhang, S. Effect of diesel pre-injection timing on combustion and emission characteristics of compression ignited natural gas engine. *Energy Convers. Manag.* **2016**, *117*, 86–94. [[CrossRef](#)]
6. Yang, B.; Wei, X.; Xi, C.; Liu, Y.; Zeng, K.; Lai, M.-C. Experimental study of the effects of natural gas injection timing on the combustion performance and emissions of a turbocharged common rail dual-fuel engine. *Energy Convers. Manag.* **2014**, *87*, 297–304. [[CrossRef](#)]
7. Zheng, J.; Wang, J.; Zhao, Z.; Wang, D.; Huang, Z. Effect of equivalence ratio on combustion and emissions of a dual-fuel natural gas engine ignited with diesel. *Appl. Therm. Eng.* **2018**, *146*, 738–751. [[CrossRef](#)]
8. Muralidharan, M.; Srivastava, A.; Subramanian, M. A Technical Review on Performance and Emissions of Compressed Natural Gas-Diesel Dual Fuel Engine. *SAE Tech. Pap.* **2019**. [[CrossRef](#)]
9. Sankaranarayanan, R.; Petersen, E.L. Laminar flame speed correlations for pure-hydrogen and high-hydrogen content syngas blends with various diluents. *Int. J. Hydrogen Energy* **2012**, *37*, 19177–19189. [[CrossRef](#)]
10. Akal, D.; Öztuna, S.; Büyükkakin, M.K. A review of hydrogen usage in internal combustion engines (gasoline-Lpg-diesel) from combustion performance aspect. *Int. J. Hydrogen Energy* **2020**, *45*, 35257–35268. [[CrossRef](#)]
11. Nag, S.; Sharma, P.; Gupta, A.; Dhar, A. Experimental study of engine performance and emissions for hydrogen diesel dual fuel engine with exhaust gas recirculation. *Int. J. Hydrogen Energy* **2019**, *44*, 12163–12175. [[CrossRef](#)]
12. Castro, N.; Toledo, M.; Amador, G. An experimental investigation of the performance and emissions of a hydrogen-diesel dual fuel compression ignition internal combustion engine. *Appl. Therm. Eng.* **2019**, *156*, 660–667. [[CrossRef](#)]

13. Zhou, J.H.; Cheung, C.H.; Leung, C.W. Combustion, performance and emissions of a diesel engine with H₂, CH₄ and H₂-CH₄ addition. *Int. J. Hydrogen Energy* **2014**, *39*, 4611–4621. [[CrossRef](#)]
14. Ouchikh, S.; Lounici, M.S.; Tarabet, L.; Loubar, K.; Tazerout, M. Effect of natural gas enrichment with hydrogen on combustion characteristics of a dual fuel diesel engine. *Int. J. Hydrogen Energy* **2019**, *44*, 13974–13987. [[CrossRef](#)]
15. Liu, F.; Kang, Y.; Wu, H.; Lee, C.-F.; Li, Y. Effect of Hydrogen Volume Ratio on the Combustion Characteristics of CNG-Diesel Dual-Fuel Engine. *SAE Tech. Pap.* **2017**. [[CrossRef](#)]
16. Tripathi, G.; Sharma, P.; Dhar, A. Computational study of diesel injection strategies for methane-diesel dual fuel engine. *Clean. Eng. Technol.* **2022**, *6*, 100393. [[CrossRef](#)]
17. Li, Y.; Li, H.; Guo, H.; Li, Y.; Yao, M. A numerical investigation on methane combustion and emissions from a natural gas-diesel dual fuel engine using CFD model. *Appl. Energy* **2017**, *205*, 153–162. [[CrossRef](#)]
18. Papagiannakis, R.G.; Hountalas, D.T.; Krishnan, S.R.; Srinivasan, K.K.; Rakopoulos, D.C.; Rakopoulos, C. Numerical evaluation of the effects of compression ratio and diesel fuel injection timing on the performance and emissions of a fumigated natural gas–diesel dual-fuel engine. *J. Energy Eng.* **2016**, *142*, E4015015. [[CrossRef](#)]
19. Mousavi, S.M.; Saray, R.K.; Poorghasemi, K.; Maghbouli, A. A numerical investigation on combustion and emission characteristics of a dual fuel engine at part load condition. *Fuel* **2016**, *166*, 309–319. [[CrossRef](#)]
20. Jabbr, A.I.; Gaja, H.; Koylu, O. Multi-objective optimization of operating parameters for a H₂/Diesel dual-fuel compression-ignition engine. *Int. J. Hydrogen Energy* **2020**, *45*, 19965–19975. [[CrossRef](#)]
21. Ramsay, C.J.; Dinesh, K.K.J.R.; Fairney, W.; Vaughan, N. A numerical study on the effects of constant volume combustion phase on performance and emissions characteristics of a diesel-hydrogen dual-fuel engine. *Int. J. Hydrogen Energy* **2020**, *45*, 32598–32618. [[CrossRef](#)]
22. Ekin, F.; Ozsoysal, O.A.; Arslan, H. The effect of using hydrogen at partial load in a diesel-natural gas dual fuel engine. *Int. J. Hydrogen Energy* **2022**, *47*, 18523–18550. [[CrossRef](#)]
23. Mansor, M.R.A.; Mohamad, T.I.; Sabah, O. Numerical investigation on combustion and emissions in a direct injection compression ignition engine fuelled with various hydrogen–methane–diesel blends at different intake air temperatures. *Energy Rep.* **2021**, *7*, 403–421. [[CrossRef](#)]
24. Sharma, P.; Dhar, A. Compression ratio influence on combustion and emissions characteristic of hydrogen diesel dual fuel CI engine: Numerical Study. *Fuel* **2018**, *222*, 852–858. [[CrossRef](#)]
25. Tripathi, G.; Sharma, P.; Dhar, A.; Sadiki, A. Computational investigation of diesel injection strategies in hydrogen-diesel dual fuel engine. *Sustain. Energy Technol. Assess.* **2019**, *36*, 100543. [[CrossRef](#)]
26. Wang, H.; Ra, Y.; Jia, M.; Reitz, R.D. Development of a reduced n-dodecane-PAH mechanism and its application for n-dodecane soot predictions. *Fuel* **2014**, *136*, 25–36. [[CrossRef](#)]
27. De Robbio, R.; Cameretti, M.C.; Mancaruso, E.; Tuccillo, R.; Vaglieco, B.M. Combined CFD-Experimental Analysis of the In-Cylinder Combustion Phenomena in a Dual Fuel Optical Compression Ignition Engine. *SAE Tech. Pap.* **2021**. [[CrossRef](#)]
28. De Robbio, R.; Cameretti, M.C.; Mancaruso, E.; Tuccillo, R.; Vaglieco, B.M. CFD Study and Experimental Validation of a Dual Fuel Engine: Effect of Engine Speed. *Energies* **2021**, *14*, 4307. [[CrossRef](#)]
29. Mancaruso, E.; Todino, M.; Vaglieco, B.M. Study on dual fuel combustion in an optical research engine by infrared diagnostics varying methane quantity and engine speed. *Appl. Therm. Eng.* **2020**, *178*, 115623. [[CrossRef](#)]
30. Mancaruso, E.; Todino, M.; Vaglieco, B.M. Analysis of Dual Fuel Combustion in Single Cylinder Research Engine Fueled with Methane and Diesel by IR Diagnostics. *SAE Tech. Pap.* **2019**. [[CrossRef](#)]
31. Magno, A.; Mancaruso, E.; Vaglieco, B.M. Combustion Analysis of Dual Fuel Operation in Single Cylinder Research Engine Fuelled with Methane and Diesel. *SAE Tech. Pap.* **2015**. [[CrossRef](#)]